Monthly Notices
of the
ROYAL ASTRONOMICAL SOCIETY

MNRAS **498,** 6057–6068 (2020)
Advance Access publication 2020 September 14

doi:10.1093/mnras/staa2769

Weak lensing skew-spectrum

D. Munshi,[1]★ T. Namikawa,[2] T. D. Kitching,[1] J. D. McEwen[1] and F. R. Bouchet[3]

[1]*Mullard Space Science Laboratory, University College London, Holmbury St Mary, Dorking, Surrey RH5 6NT, UK*
[2]*Department of Applied Mathematics and Theoretical Physics, University of Cambridge, Wilberforce Road, Cambridge CB3 OWA, UK*
[3]*Institut d'Astrophysique de Paris, UMR 7095, CNRS & Sorbonne Universit, 98 bis Boulevard Arago, F-75014 Paris, France*

Accepted 2020 September 7. Received 2020 September 7; in original form 2020 June 25

ABSTRACT

We introduce the skew-spectrum statistic for weak lensing convergence κ maps and test it against state-of-the-art high-resolution all-sky numerical simulations. We perform the analysis as a function of source redshift and smoothing angular scale for individual tomographic bins. We also analyse the cross-correlation between different tomographic bins. We compare the numerical results to fitting-functions used to model the bispectrum of the underlying density field as a function of redshift and scale. We derive a closed form expression for the skew-spectrum for gravity-induced secondary non-Gaussianity. We also compute the skew-spectrum for the projected κ inferred from cosmic microwave background (CMB) studies. As opposed to the low redshift case, we find the post-Born corrections to be important in the modelling of the skew-spectrum for such studies. We show how the presence of a mask and noise can be incorporated in the estimation of a skew-spectrum.

Key words: Cosmology – Weak Lensing – Methods: analytical, statistical, numerical.

1 INTRODUCTION

Recently completed cosmic microwave background (CMB) experiments such as the Planck Surveyor[1] (Planck Collaboration XVI 2014; Planck Collaboration VI 2018), have helped establishing a standard model of cosmology, with the baseline cosmological parameters now known with an unprecedented accuracy. However, many fundamental questions in cosmology remain open. These include the nature of dark matter and dark energy, a possible modification of General Relativity on cosmological scales (Clifton et al. 2012; Joyce et al. 2014) and the nature of neutrinos mass hierarchy (Lesgourgues & Pastor 2006). Next generation of large-scale surveys will provide a massive amount of high-precision data carrying complementary information that can help answer at least some of these questions. Indeed, observational programs of many ongoing as well as future surveys including the surveys e.g. *Euclid*[2] (Laureijs et al 2006), CFHTLS,[3] PAN-STARRS,[4] Dark Energy Surveys[5] (Allam et al. 2016), WiggleZ[6] (Drinkwater et al. 2010), Rubin Observatory,[7] (Tyson et al. 2003), BOSS[8] (Eisenstein et al. 2011), KIDS (Kuijken et al. 2015), *Roman Space Telescope* (National Research Council 2010), lists weak lensing as their main science driver. From the early days of detection weak lensing (see e.g. Munshi et al. 2008 for a review) studies have now reached a level of maturity. Surveys such as *Euclid* will constrain the cosmological parameters with sub-per cent accuracy and answer many of the most challenging questions that cosmology is facing today.

Weak lensing at smaller angular scales probes scales that are in the highly non-linear regime and contains a wealth of cosmological information. This gravity-induced non-linearity (Bernardeau et al. 2002) introduces mode-coupling that is responsible for the resulting departure from Gaussianity (Bartolo et al. 2004). Higher order statistics beyond power spectrum estimation is typically used in exploitation of the information content of weak lensing maps. An accurate modelling of higher order statistics is important for modelling the covariance of the lower order estimators as well as to break cosmological parameter degeneracy. Early studies of higher order statistics concentrated on cumulants (Bernardeau 1994a, b) in real-space (Bernardeau, Mellier & van Waerbeke 2002; Bernardeau, van Waerbeke & Mellier 2003). Future surveys such as *Euclid* will have a near all-sky coverage and thus enable quantifying higher order statistics in the harmonic domain where measurements of individual modes will be less correlated (Amendola et al. 2013).

Most theoretical modelling in the highly non-linear regime were based on perturbative calculations or its extensions (Bernardeau et al. 2002), variants of the halo models (Cooray et al. 2002), effective field theory (EFT; Baumann 2012), or fitting-functions that are calibrated from simulations (Scoccimarro & Frieman 1999; Gil-Marin et al. 2012). Many different estimators are currently available for analysing departures from Gaussianity, including morphological estimators (Munshi et al. 2012), position-dependent power spectra (Munshi et al. 2020b), line-correlations (Eggemeier & Smith 2017), extreme value statistics (Harrison & Coles 2011). peak-statistics (Kacprzak et al. 2016; Shan et al. 2018), void statistics (Krause et al. 2013), and probability distribution functions (Codis et al. 2016; Uhlemann et al. 2016; Valageas 2016; Gruen et al. 2018).

★ E-mail: d.munshi@ucl.ac.uk
[1]http://sci.esa.int/planck/
[2]http://sci.esa.int/euclid/
[3]http://www.cfht.hawai.edu/Sciences/CFHLS
[4]http://pan-starrs.ifa.hawai.edu/
[5]https://www.darkenergysurvey.org/
[6]http://wigglez.swin.edu.au/
[7]http://www.lsst.org/llst/home.shtml
[8]http://www.sdss3.org/surveys/boss.php

The measurements of angular correlations have the benefit of simplicity especially while the survey geometry (mask) is complicated (Munshi & Jain 2001, 2000; Munshi 2000). However, such measurements are highly correlated. In contrast, the measurements in the harmonic domain are less correlated and contain independent information especially when the sky coverage is high. One of the motivation of this study is to develop analytical predictions for one such proxy statistics to the bispectrum called skew-spectrum (Cooray 2001; Munshi & Heavens 2010) and test them against state-of-art numerical simulations. We will borrow the concepts developed for constructing skew-spectrum for the study of non-Gaussianity in the context of cosmic microwave background (CMB) observations by *WMAP*[9] (Smidt et al. 2010; Calabrese et al. 2010) and *Planck* (Planck Collaboration XIII 2016a, b) satellites. However our aim here is also to include gravity-induced secondary non-Gaussianity. The skew-spectrum is the lowest order member in the family of higher order spectra (Munshi et al. 2011a,b). They can also be used to reconstruct morphological estimators, e.g. Minkowski Functionals, in an order by order manner in the presence of complicated survey topology (Munshi et al. 2012). Recently the skew-spectrum statistics was used to study the possibility of probing galaxy clustering using data from the forthcoming generation of wide-field galaxy surveys (Schmittfull, Baldauf & Seljak 2015; Dai, Verde & Xia 2019; Dizgah et al. 2020).

In this paper, we show that the skew-spectrum statistics can be used to analyse the weak lensing maps that will be available from the future stage-IV experiments such as *Euclid* or the Rubin Observatory. We also show how the suboptimal skew-spectrum can be used to probe the gravity-induced non-Gaussianity of the reconstructed convergence maps from CMB observations. We will present the skew-spectrum by cross-correlating different tomographic bins as well as the CMB convergence maps and the low redshift weak lensing convergence maps. In this context, we will emphasize the importance of the post-Born corrections in theoretical modelling of the bispectrum. Finally, we will consider many modified theories of gravity and use second-order perturbation theory to model the theoretical skew-spectrum at large smoothing angular scales to provide an example of important science goals that can be achieved using the skew-spectrum statistics.

This paper is organized as follows. In Section 2, we briefly review the modelling of the density bispectrum. In Section 3, we introduce our notations and briefly summarize the results of projected weak lensing convergence or κ bispectrum. The Section 4 is devoted to the discussion of the simulations we use in our study. In Section 5, we present the estimator we use. The results are discussed in Section 6 and conclusion and future prospects are presented in Section 7.

2 MODELLING OF THE DENSITY BISPECTRUM

We discuss relevant aspects of the tree-level perturbation theory in this section. We also discuss extensions based on fitting-function, which we use to compute the bispectrum and eventually the skew-spectrum.

2.1 Tree-level perturbative calculations

In the weakly non-linear regime with density contrast ($\delta \leq 1$), the gravitational clustering can be described by the Eulerian perturbation theory (Munshi et al. 2008). However, the treatment eventually breaks down when δ becomes non-linear ($\delta \geq 1$). Expanding δ in a Fourier series, and assuming $\delta \leq 1$, for the pertubative series to be convergent, we get

$$\delta(\mathbf{k}) = \delta^{(1)}(\mathbf{k}) + \delta^{(2)}(\mathbf{k}) + \delta^{(3)}(\mathbf{k}) + \ldots; \tag{1a}$$

$$\delta^{(2)}(k) = \int \frac{\mathrm{d}^3\mathbf{k}_1}{2\pi} \int \frac{\mathrm{d}^3\mathbf{k}_2}{2\pi} \delta_D(\mathbf{k_1} + \mathbf{k_2} - \mathbf{k}) F_2(\mathbf{k}_1, \mathbf{k}_2) \delta^{(1)}(\mathbf{k}_1) \times \delta^{(1)}(\mathbf{k}_2); \tag{1b}$$

$$F_2(\mathbf{k}_1, \mathbf{k}_2) = \frac{5}{7} + \frac{1}{2}\left(\frac{k_1}{k_2} + \frac{k_2}{k_1}\right)\left(\frac{\mathbf{k}_1 \cdot \mathbf{k}_2}{k_1 k_2}\right) + \frac{2}{7}\left(\frac{\mathbf{k}_1 \cdot \mathbf{k}_2}{k_1 k_2}\right)^2. \tag{1c}$$

The linearized solution for δ will be denoted by $\delta^{(1)}(\mathbf{k})$; higher order terms $\delta^{(2)}$, $\delta^{(3)}$, $\cdots$ will denote the second- and third-order corrections to the linear solution. The 3D wave vectors are denoted as $\mathbf{k}$, $\mathbf{k}_1$, $\mathbf{k}_2$, and their magnitudes as $k = |\mathbf{k}|$ and $k_i = |\mathbf{k}_i|$. More details of our Fourier convention will be introduced in Section 3.2. Our Eulerian formalism is based on a perfect-fluid approach. This is valid at large scales (i.e. before shell crossing). We will be taking the fitting-function approach in the non-perturbative regime. in recent years many new methods have been developed to tackle the gravitational instability in the non-linear regime including EFT methods (see e.g. Munshi & Regan 2012 and references therein).

2.2 Phenomenological fitting-functions

Beyond the quasi-linear regime non-perturbative tools become necessary. One such approach was developed in Scoccimarro & Frieman (1999) who proposed the so-called Hyper Extended Perturbation Theory (HEPT) in the highly non-linear regime and a fitting-function that connects it with the tree-level perturbative calculation. The fitting function which interpolates these two regime is calibrated using numerical simulations. Over the years similar but more accurate fitting formula were developed by other authors (Gil-Marin et al. 2012), which essentially generalize the kernel F_2 defined in equation (1c) by introducing scale-dependent coefficients $a(n_i, k_i)$, $b(n_j, k_j)$, and $c(n_j, k_j)$:

$$F_2(\mathbf{k}_i, \mathbf{k}_j) = \frac{5}{7} a(n_i, k_i) a(n_j, k_j) + \frac{1}{2}\left(\frac{\mathbf{k}_i \cdot \mathbf{k}_j}{k_i k_j}\right)\left(\frac{k_i}{k_j} + \frac{k_j}{k_i}\right) \times b(n_i, k_i) b(n_j, k_j) + \frac{2}{7}\left(\frac{\mathbf{k}_i \cdot \mathbf{k}_j}{k_i k_j}\right)^2 c(n_i, k_i)\, c(n_j, k_j). \tag{2}$$

Here n_e is the effective spectral slope associated with the linear power spectra $n_e = d \ln P_\delta(k)/d \ln k$, q is the ratio of a given length scale to the non-linear length scale $q = k/k_{\rm nl}$, where $k_{\rm nl}^3/2\pi^2 D_+^2(z) P_\delta(k_{\rm nl}) = 1$. Here $D_+(z)$ represents the linear growth rate of perturbations at redshift z. At length scales where $q \ll 1$, the relevant length scales are well within the quasi-linear regime, $a = b = c = 1$, and we recover the tree-level perturbative results. In the regime where $q \gg 1$, and the length scales we are considering are well within the non-linear scale, we recover $a \neq 1$ but $b = c = 0$. In this limit, the bispectrum becomes independent of configuration. It was recently pointed out by Munshi et al. (2020a) that the fitting function of Gil-Marin et al. (2012) is not very accurate in describing the weak lensing bispectrum. A more accurate fitting function was developed recently in Takahasi et al. (2020) which we will be using in this study. The original fitting function by (Scoccimarro & Frieman 1999) involved

[9] https://map.gsfc.nasa.gov/

just six free parameters and was valid for $k < 3h\mathrm{Mpc}^{-1}$ and $0 < z < 1$. The improved (Gil-Marin et al. 2012) formula has a limited range of validity $k < 0.4h\mathrm{Mpc}^{-1}$ and $0 < z < 1.5$ and contains nine parameters. The fitting function by Takahasi et al. (2019) contains 52 free parameters. Introduction of such a large number of free parameters increases the validity range to $k = 10h\mathrm{Mpc}^{-1}$ and $z \approx 1$–3. This will be important in modelling non-Gaussianity on arcminute scales probed by the future stage-IV experiments.

3 WEAK LENSING STATISTICS IN PROJECTION

In this section, we will relate the convergence bispectrum κ with its 3D density contrast δ counterpart. Then this bispectrum will be used to construct the convergence skew-spectrum.

3.1 Projected weak lensing bispectrum

The weak lensing convergence κ and 3D density contrast $\delta(\mathbf{r})$ is related by the following expression:

$$\kappa(\boldsymbol{\theta}) := \int_0^{r_s} \mathrm{d}r\, w(r)\delta(r, \boldsymbol{\theta});$$
$$w(r) := \frac{3\Omega_\mathrm{M}}{2}\frac{H_0^2}{c^2}a^{-1}\frac{d_A(r)d_A(r_s - r)}{d_A(r_s)}. \tag{3}$$

We have introduced a kernel $w(r)$ above. In this expression, $r = |\boldsymbol{r}|$ is the comoving radial distance to the source, $\boldsymbol{\theta}$ describes the angular position on the sky, Ω_M is the cosmological matter density parameter (total matter density in units of the critical density), H_0 is the Hubble constant, c is the speed of light, $a = 1/(1 + z)$ is the scale factor at a redshift z, $d_A(r)$ represents the comoving angular diameter distance at a distance r and r_s is the comoving radial distance to the source plane. The corresponding redshift will be represented by z_s. To keep the analysis simple, in our study we will ignore the source distribution and assume them to be localized on a single source plane defined by z_s. We will study various statistics as a function of z_s. To simplify the analysis, we will also ignore photometric redshift errors. Throughout we will use the flat-sky approximation (Kilbinger et al. 2017; Kitching et al. 2017). Needless to say, such complications are essential to link predictions to observational data, and will be presented in an acompanying study.

Fourier decomposing δ along and perpendicular to the line-of-sight direction we obtain:

$$\kappa(\boldsymbol{\theta}) = \int_0^{r_s} \mathrm{d}r\omega(r) \int \frac{\mathrm{d}k_\parallel}{2\pi} \int \frac{\mathrm{d}^2\mathbf{k}_\perp}{(2\pi)^2} \times \exp[\mathrm{i}(rk_\parallel + d_A(r)\,\boldsymbol{\theta}\cdot\mathbf{k}_\perp)]\delta(\mathbf{k}; r). \tag{4}$$

Here, we have decomposed the 3D wavenumber $\mathbf{k}$ along and perpendicular to the radial direction, $\mathbf{k} = (k_{\shortparallel}, \mathbf{k}_\perp)$. We have used the following convention for the 3D Fourier Transform and its inverse:

$$\delta(\mathbf{k}) = \frac{1}{(2\pi)^3}\int \mathrm{d}^3\mathbf{r}\exp(-i\mathbf{k}\cdot\mathbf{r})\delta(\mathbf{r});$$
$$\delta(\mathbf{r}) = \int \mathrm{d}^3\mathbf{k}\exp(i\,\mathbf{r}\cdot\mathbf{k})\delta(\mathbf{k}). \tag{5}$$

The corresponding 3D power spectrum and bispectrum for δ are:

$$\langle\delta(\mathbf{k}_1)\delta(\mathbf{k}_2)\rangle_c := (2\pi)^3\delta_{3\mathrm{D}}(\mathbf{k}_1 + \mathbf{k}_2)P_\delta(k_1); \quad k = |\mathbf{k}|; \tag{6}$$

$$\langle\delta(\mathbf{k}_1)\delta(\mathbf{k}_2)\delta(\mathbf{k}_3)\rangle_c := (3\pi)^2\delta_{3\mathrm{D}}(\mathbf{k}_1 + \mathbf{k}_2 + \mathbf{k}_3)B_\delta(\mathbf{k}_1, \mathbf{k}_2, \mathbf{k}_3). \tag{7}$$

Using the small-angle approximation the projected power spectrum $P^\kappa(l)$ and bispectrum $B^\kappa(\mathbf{l}_1, \mathbf{l}_2, \mathbf{l}_3)$ of the convergence field κ can be expressed respectively in terms of the 3D power spectrum $P_\delta(k)$ and bispectrum $B_\delta(\mathbf{k}_1, \mathbf{k}_2, \mathbf{k}_3)$:

$$P^\kappa(l) = \int_0^{r_s} \mathrm{d}r\frac{\omega^2(r)}{d_A^2(r)}P_\delta\left(\frac{l}{d_A(r)}; r\right); \tag{8a}$$

$$B^\kappa(\mathbf{l}_1, \mathbf{l}_2, \mathbf{l}_3) = \int_0^{r_s} \mathrm{d}r\frac{\omega^3(r)}{d_A^4(r)}B_\delta\left(\frac{\mathbf{l}_1}{d_A(r)}, \frac{\mathbf{l}_2}{d_A(r),}, \frac{\mathbf{l}_3}{d_A(r)}; r\right). \tag{8b}$$

Detailed derivations of these expressions can be found in Munshi et al. (2008). Cross-correlating two-tomographic bins can be used to define cross-spectra $P^\kappa_{\alpha\beta}$ and cross-skew spectra $B^\kappa_{\alpha\beta}$.

$$P^\kappa_{\alpha\beta}(l) = \int_0^{r_\mathrm{min}} \mathrm{d}r\frac{\omega_\alpha(r)\omega_\beta(r)}{d_A^2(r)}P_\delta\left(\frac{l}{d_A(r)}; r\right); \tag{9a}$$

$$B^\kappa_{\alpha\beta}(\mathbf{l}_1, \mathbf{l}_2, \mathbf{l}_3) = \int_0^{r_\mathrm{min}} \mathrm{d}r\frac{\omega^1_\alpha(r)\omega^2_\beta(r)}{d_A^4(r)} \times B_\delta\left(\frac{\mathbf{l}_1}{d_A(r)}, \frac{\mathbf{l}_2}{d_A(r),}, \frac{\mathbf{l}_3}{d_A(r)}; r\right);$$
$$r_\mathrm{min} = min(r_\alpha, r_\beta); \tag{9b}$$

$$w_i(r) := \frac{3\Omega_\mathrm{M}}{2}\frac{H_0^2}{c^2}a^{-1}\frac{d_A(r)d_A(r_{si} - r)}{d_A(r_{si})}; \quad i \in \{\alpha, \beta\}. \tag{9c}$$

The integration takes contribution only from the overlapping redshift range of the two bins. Thus, the upper limit extends only to the source plane defined by the lower redshift $r_\mathrm{min} = \min(r_\alpha, r_\beta)$. Notice that $P^\kappa_{\alpha\beta} = P^\kappa_{\beta\alpha}$ but $B^\kappa_{\alpha\beta} \neq B^\kappa_{\beta\alpha}$ and they carry independent information. It is possible to directly deal with shear bispectrum and relate them to density bispectrum thus avoiding the map making process. See Munshi et al. (2011d) for bispectra constructed for higher spin objects, i.e. shear as well as flexions.

3.2 Skew-spectrum in all-sky and flat-sky

The skew-spectrum statistic for κ is constructed by cross-correlating the squared κ with itself. We start by introducing the spherical harmonic transform of a convergence map $\kappa(\hat{\Omega})$ defined over the surface of the sky using spherical harmonics $Y_{\ell m}(\hat{\Omega})$ to define the multipoles $\kappa_{\ell m}$:

$$\kappa_{\ell m} := \int \mathrm{d}\hat{\Omega}\, Y_{\ell m}\,\kappa(\hat{\Omega}); \quad \hat{\Omega} = (\vartheta, \varphi); \quad \mathrm{d}\hat{\Omega} = \sin\vartheta\,\mathrm{d}\vartheta\,\mathrm{d}\varphi. \tag{10}$$

Any Gaussian field is completely characterized by its power spectrum $\mathcal{C}^\kappa_\ell$ which is defined as $\mathcal{C}^\kappa_\ell := \langle\kappa_{\ell m}\kappa^*_{\ell m}\rangle$. In the flat-sky limit the power spectrum $P^\kappa(l)$ is identical to $\mathcal{C}^\kappa_\ell$ at high ℓ with the identification $l = \ell$. The weak lensing κ maps are highly non-Gaussian. The bispectrum characterizes departure from Gaussianity and is defined as the three-point coupling of harmonic coefficients. The statistics beyond bispectra, e.g. the trispectra and its higher order analogues are increasingly noise dominated. By assuming isotropy and homogeneity the all-sky bispectrum $B^\kappa_{\ell_1\ell_2\ell_3}$ is defined as

$$\langle\kappa_{\ell_1 m_1}\kappa_{\ell_2 m_2}\kappa_{\ell_3 m_3}\rangle_c \equiv B^\kappa_{\ell_1\ell_2\ell_3}\begin{pmatrix}\ell_1 & \ell_2 & \ell_3\\ 0 & 0 & 0\end{pmatrix}. \tag{11}$$

The Wigner-3j symbol appearing above in parentheses ensures rotational invariance. It is only non-zero for the triplets (ℓ_1, ℓ_2, ℓ_3) that satisfy the triangular condition and $\ell_1 + \ell_2 + \ell_3$ is even. The reduced bispectrum $b^\kappa_{\ell_1\ell_2\ell_3}$ is useful in directly linking the all-sky bispectrum and its flat-sky counterpart. For the convergence field κ,

$b^{\kappa}_{\ell_1\ell_2\ell_3}$ is defined through the following expression:

$$B^{\kappa}_{\ell_1\ell_2\ell_3} := \sqrt{\frac{(2\ell_1+1)(2\ell_2+1)(2\ell_3+1)}{4\pi}} \begin{pmatrix} \ell_1 & \ell_2 & \ell_3 \\ 0 & 0 & 0 \end{pmatrix} b^{\kappa}_{\ell_1\ell_2\ell_3}. \tag{12}$$

Finally we are in a position to define the skew spectrum as the cross power-spectra formed by cross-correlating the squared $\kappa^2(\hat{\Omega})$ maps against the original map $\kappa(\hat{\Omega})$.

$$\mathcal{S}_\ell := \frac{1}{2\ell+1}\sum_m \text{Real}\left\{[\kappa^2]_{\ell m}[\kappa]^*_{\ell m}\right\} = \sum_{\ell_1\ell_2} B^{\kappa}_{\ell_1\ell_2\ell} J_{\ell_1\ell_2\ell}; \tag{13a}$$

$$J_{\ell_1\ell_2\ell} := \sqrt{\frac{(2\ell_1+1)(2\ell_2+1)}{4\pi(2\ell+1)}} \begin{pmatrix} \ell_1 & \ell_2 & \ell \\ 0 & 0 & 0 \end{pmatrix}. \tag{13b}$$

Here $[\kappa^2]_{\ell m}$ represents the harmonic multipoles computed using a harmonic decomposition of κ^2 and * denotes complex conjugation. The commonly used (normalized) one-point skewness parameter $S_3 = \langle\kappa^3\rangle_c/\langle\kappa^2\rangle_c^2$ can be recovered from the skew-spectrum. The third-order moment $\langle\kappa^3\rangle$ is given by:

$$\langle\kappa^3(\theta_s)\rangle_c = \frac{1}{4\pi}\sum_\ell (2\ell+1) S_\ell \beta^3_\ell(\theta_s); \tag{14}$$

The smoothing beam (window) is denoted as $\beta_\ell(\theta_s)$. Being a two-point statistic, the skew-spectrum S_ℓ is related to the two-to-one correlation function ξ^{21} in the real space. They are related by the following expression:

$$\xi^{21}(\theta_{12}) := \langle\kappa^2(\theta_1)\kappa(\theta_2)\rangle_c = \frac{1}{4\pi}\sum_\ell (2\ell+1) S_\ell P_\ell(\cos\theta_{12})\beta^3_\ell(\theta_s). \tag{15}$$

Here P_ℓ is the Legendre Polynomial and β_ℓ is the Gaussian smoothing beam with full width at half-maximum (FWHM) of θ_s. Suitably normalized two-to-one correlators the lowest order of a family of statistics also known as cumulant correlator (Bernardeau 1996), it has also been used in the context of weak-lensing surveys (Munshi 2000). The flat-sky bispectrum is similarly defined through:

$$\langle\kappa(\mathbf{l}_1)\kappa(\mathbf{l}_2)\kappa(\mathbf{l}_3)\rangle_c = (2\pi)^2\delta_{2D}(\mathbf{l}_1+\mathbf{l}_2+\mathbf{l}_3)B^{\kappa}(\mathbf{l}_1,\mathbf{l}_2,\mathbf{l}_3). \tag{16}$$

The flat-sky bispectrum $B^{\kappa}(\mathbf{l}_1, \mathbf{l}_2, \mathbf{l}_3)$ is identical to the reduced bispectrum $b_{\ell_1\ell_2\ell_2}$ for high multipole (Bartolo et al. 2004). This can be shown by using the following asymptotic relationship:

$$\begin{aligned}\mathcal{G}_{\ell_1 m_1,\ell_2 m_2,\ell_3 m_3} &\equiv \int \mathrm{d}\hat{\Omega} Y_{\ell_1 m_1}(\hat{\Omega}) Y_{\ell_2 m_2}(\hat{\Omega}) Y_{\ell_3 m_3}(\hat{\Omega}) \\ &= \sqrt{\frac{(2\ell_1+1)(2\ell_2+1)(2\ell+1)}{4\pi}} \\ &\quad\times \begin{pmatrix} \ell_1 & \ell_2 & \ell \\ 0 & 0 & 0 \end{pmatrix} \begin{pmatrix} \ell_1 & \ell_2 & \ell \\ m_1 & m_2 & m_3 \end{pmatrix} \\ &\approx (2\pi)^2\delta_{2\mathrm{D}}(\mathbf{l}_1+\mathbf{l}_2+\mathbf{l}_3).\end{aligned} \tag{17a}$$

The skew-spectrum in the flat-sky is given by (Pratten & Munshi 2012):

$$\begin{aligned}\mathcal{S}(l_2) = \int_0^\infty \frac{l_1\mathrm{d}l_1}{2\pi}\int_{-1}^{1}\frac{\mathrm{d}\mu}{2\pi\sqrt{1-\mu^2}} \\ \times B^{\kappa}(\mathbf{l}_1,\mathbf{l}_2,-(\mathbf{l}_1+\mathbf{l}_2))\beta(l_1\theta_s)\beta(l_2\theta_s)\beta(|\mathbf{l}_1+\mathbf{l}_2|\theta_s).\end{aligned} \tag{18}$$

In our notation $\mu = (\mathbf{l}_1\cdot\mathbf{l}_2/l_1l_2)$, and we have used $\beta_{\ell_1}(\theta_s) = \beta(l_1\theta_s)$ to denote the flat-sky beam. In the high-l limit we have $\mathcal{S}(l_2) \to S_{\ell_2}$.

Here a few comments about the skew-spectrum are in order. The skewness has a high signal to noise. However, it lacks distinguishing power. Therefore, such statistics cannot distinguish various contributions, e.g. from primordial non-Gaussianity or non-Gaussianity from intrinsic alignment of source galaxies from the gravity-induced secondary non-Gaussianity. The skew-spectrum, on the other hand, retains some of the information regarding the shape of the spectrum, thus it can, in principle, allow us to separate various contributions or remove possible source of contamination from systematics.

We consider a direct estimator in this paper. Optimality can be achieved by using suitable weights (Komatsu, Spergel & Wandelt 2005; Munshi & Heavens 2010). However, optimality is not of crucial importance for analysing weak lensing maps as the secondary non-Gaussianity is expected to be detected with a very high signal to noise. A direct estimator, which is simpler to implement, will thus be useful for studying non-Gaussianity in weak lensing maps.

A few comments are in order. The skewness, skew-spectrum, and bispectrum are all third-order statistics. However, their information contents are not the same. The skewness is an one-point statistics which can be constructed from the skew-spectrum. The skew-spectrum being a two-point statistics cannot however be constructed from the skewness. Similarly bispectrum is a Fourier (or harmonic) analogue of the three-point correlation function. Being a three-point statistics it cannot be constructed from the skew-spectrum and contains more information. The use of skew-spectrum can be treated as a data compression step as computation of the entire covariance matrix of the bispectrum can be a challenging task. Indeed the bispectrum, skew-spectrum, and skewness are equally sensitive to the second-order non-linearities. However, the skewness cannot distinguish among different contributions from various sources of non-linearities that the skew-spectrum is able to do. Physically skew-spectrum is the Fourier (or harmonic) transform of the two-to-one correlation function as defined in equation (15).

Next we consider skew-spectrum for specific models of bispectrum considered in Section 2.

3.3 The skew-spectrum in the tree-level standard perturbation theory (SPT)

Analytical predictions for the skew-spectrum for large smoothing angular scales can be obtained using perturbative calculations. The low ℓ limit of the skew-spectrum and its higher order generalizations were recently presented in Munshi & McEwen (2020). This is possible using a technique based on a generating function formalism. However, for arbitrary ℓ an order-by-order calculation is needed. We will obtain these results using a Gaussian smoothing beam where complete analytical results in closed form can be derived. We will consider the gravity-induced (secondary) non-Gaussianity.

$$\begin{aligned}S(l_2) = \int \mathrm{d}r\ \frac{w^3(r)}{d_A^4(r)}\int\frac{l_1\mathrm{d}l_1}{(2\pi)^2}P_\delta\left(\frac{l_1}{d_a(r)};r\right)P_\delta\left(\frac{l_2}{d_a(r)};r\right) \\ \times\beta^2(l_1\theta_s)\beta^2(l_2\theta_s)\mathcal{T}(l_1l_2)\end{aligned} \tag{19a}$$

$$\begin{aligned}\mathcal{T}(l_1l_2) = \left[\frac{36}{7}I_0\left(l_1l_2\theta_s^2\right) - 3\left(\frac{l_1}{l_2}+\frac{l_2}{l_1}\right)\right. \\ \left.\times I_1\left(l_1l_2\theta_s^2\right) + \frac{6}{7}I_2\left(l_1l_2\theta_s^2\right)\right].\end{aligned} \tag{19b}$$

The angular integral in equation (18) can be done analytically using the modified Bessel functions represented in I_m. To simplify the notation we adopt a parametrization in terms of the variables $C_m^{\alpha\beta}$:

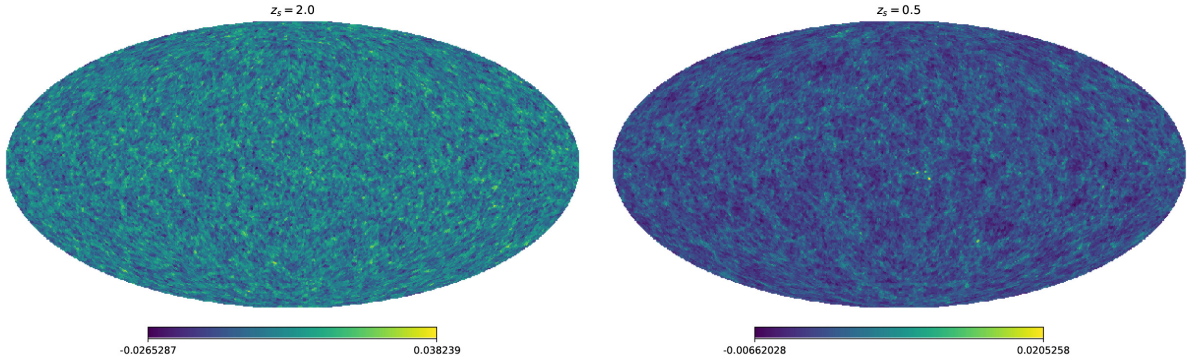

Figure 1. Examples of realizations of all-sky weak lensing convergence or κ maps used for our study. The left- and right-panel panels correspond, respectively, source redshift $z_s = 2.0$ and 0.5. The κ maps, we have used, were generated at a HEALPIX resolution $N_{\rm side} = 4096$, and we have degraded them to $N_{\rm side} = 2048$ for our study.

$$S(l_2) = \sigma_L^2 P^\kappa(l_2) R_2 \int \frac{l_1 {\rm d}l_1}{2\pi} l_1^n l_2^n \beta^2(l_1\theta_s)\beta^2(l_2\theta_s)\mathcal{T}(l_1 l_2); \tag{20a}$$

$$R_2 = \int_0^{r_s} {\rm d}r \frac{w^3(r)}{d_A^{4+2n}(r)} D_+^4(z) / \left[\int_0^{r_s} {\rm d}r \frac{w^2(r)}{d_A^{2+n}(r)} D_+^2(z)\right]^2 . \tag{20b}$$

To separate the temporal r and angular l parts of the integral, we replaced the linear power spectrum $P_\delta(k)$ with a power-law form, i.e. $P_\delta(k) = A D_+^2(z) k^n$. Due to the choice of normalization here the skew-spectrum is independent of the power spectrum amplitude A. The resulting skewness S_3 can then be written as

$$S_3 := \int l_2 \, {\rm d}\, l_2 \, S(l_2) \qquad . \tag{21}$$

The F_2 kernel for many modified gravity theories have a similar structural form and can be treated analytically. Similarly, the EFT based approaches introduces corrective terms to F_2 that too have a very similar form (Munshi & Regan 2012). The kernel describing the primordial non-Gaussianity can also be treated in a similar manner. We will focus on certain well-known cases of modified gravity theories. The analytical results for these models are important as there are no established numerical fitting-function available in these scenarios.

4 NUMERICAL SIMULATIONS

The simulated all-sky maps we have used in our study are available for public use (Takahashi et al. 2017).[10] Ray-tracing through numerical (N-body) simulation were used to generate these maps. The underlying simulations followed the gravitational clustering of 2048^3 particles. The lensing maps were generated using multiple lens planes. A range of source redshifts were used $z_s = 0.05$–5.30 with $\Delta z_s = 0.05$. In our numerical study, we have used the maps with source redshifts $z_s = 0.5$, 1.0, 1.5, 2.0. For CMB maps, the lensing potentials were constructed using the deflection angles which were used to construct the lensing potentials and eventually the κ maps. In recent studies inclusion of post-Born terms in lensing statistics were outlined (Pratten & Lewis 2016). The maps we use include post-Born corrections. In this study, we will see that at a low source redshift such corrections do not play any significant role although they do play an important role at higher redshifts, e.g. in case of lensing of CMB. The `healpix`[11] (Gorski et al. 2005) equal area pixelization scheme was used in generating these maps. The number of pixels denoted by $N_{\rm pix}$ scale as $N_{\rm pix} = 12 N_{\rm side}^2$ where $N_{\rm side}$ is the parameter that defines the resolution which take values $N_{\rm side} = 2^N$ with $N = 1, 2, \cdots$. The set of maps we use in this study are generated at $N_{\rm side} = 4096$ and were cross-checked against higher resolution maps. These maps constructed at different $N_{\rm side}$ were found to be consistent with each other up to the angular harmonics $\ell \leq 2000$. Various additional tests were performed including the Electric/Magnetic (E/B) decomposition of the shear maps for the construction of κ maps (Takahashi et al. 2017). We have used high resolution maps generated at $N_{\rm side} = 4096$ and degraded them to $N_{\rm side} = 2048$ to analyse them for harmonic modes satisfying $\ell < 2N_{\rm side}$. The background cosmological parameters used for these simulations are: $\Omega_{\rm CDM} = 0.233$, $\Omega_b = 0.046$, $\Omega_{\rm M} = \Omega_{\rm CDM} + \Omega_b$, $\Omega_\Lambda = 1 - \Omega_{\rm M}$ and $h = 0.7$. The amplitude of density fluctuation $\sigma_8 = 0.82$ and the spectral index $n_s = 0.97$. Fig. 1 shows examples of maps used in numerical study. Several authors have used these maps in the context of CMB lensing (Namikawa et al. 2019) and for weak lensing of galaxies at low redhifts (Munshi et al. 2020a; Munshi & McEwen 2020).

5 THE PSEUDO SKEW-SPECTRUM ESTIMATOR

An inverse covariance weighting is needed in the construction of an optimal maximum likelihood (ML) estimator or a quadratic maximum likelihood (QML) estimator (Efsthathiou 2004). For high resolution maps the size of the data vector, however, makes these estimators difficult to implement (Oh, Spergel & Hinshaw 1990). As a result many suboptimal estimators, which use heuristic weighting schemes, have been developed. The so-called pseudo-$\mathcal{C}_\ell$ (PCL) technique was introduced in Hivon et al. (2002) in the harmonic domain. Later a related correlation function based approach was introduced in Szapudi et al. (2001). These estimators are unbiased but are suboptimal. Typically various heuristic weighting depending on sky coverage, as well as noise characteristics can improve the optimality of these estimators typically in noise dominated high-ℓ (or smaller angular scales) regime. The maximum likelihood estimators, on the other hand, can be efficiently used for larger smoothing scales. Different hybridization schemes can be used to combine the large

[10] http://cosmo.phys.hirosaki-u.ac.jp/takahasi/allsky_raytracing/

[11] https://healpix.jpl.nasa.gov/

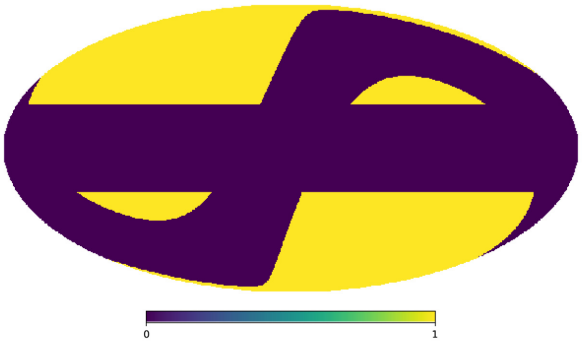

Figure 2. In our study, we use a 'pseudo Euclid' mask. In constructing the mask, all pixels (shown in dark) lying within 22 deg of either the galactic or ecliptic planes are discarded. The remaining unmasked pixels (shown in yellow) cover 14 490 deg^2 of the sky, making fraction of the sky covered $f_{\rm sky} \approx 0.35$.

angular scale (equivalently the low ℓ) estimates using QML with small angular scale (high ℓ) PCL estimates (Efsthathiou 2004). In our study, we will use a direct pseudo-$\mathcal{C}_\ell$ estimator for the skew-spectrum. The direct estimator from the masked sky $\tilde{S}_\ell$ is related to the underlying all-sky S_ℓ skew-spectrum through a mode-mixing matrix $M_{\ell\ell'}$ that depends on the mask.

$$\tilde{S}_\ell = M_{\ell\ell'} S_\ell; \quad \hat{S}_\ell = M^{-1}_{\ell\ell'} \tilde{S}_\ell; \quad \langle \hat{S}_\ell \rangle = S_\ell. \tag{22a}$$

Here $\tilde{\mathcal{S}}^{(21)}_{\ell'}$ denotes the skew-spectrum computed from a map in the presence of a mask $w(\hat{\Omega})$, $\hat{\mathcal{S}}^{(21)}_{\ell'}$ is the all-sky estimate. The mode-coupling matrix $M_{\ell\ell'}$ is given in terms of the power spectrum of the mask $w(\hat{\Omega})$ as follows:

$$M_{\ell\ell'} = (2\ell'+1) \sum_{\ell''} \begin{pmatrix} \ell & \ell' & \ell'' \\ 0 & 0 & 0 \end{pmatrix}^2 \frac{(2\ell''+1)}{4\pi} |w^2_{\ell''}|. \tag{23}$$

Here $w_\ell = 1/(2\ell+1) \sum_m w_{\ell m} w^*_{\ell m}$ is the power spectrum of the mask constructed from the harmonic-coefficient $w_{\ell m}$ of the map. The coupling matrix $M_{\ell\ell'}$ encodes the mode-mixing due to the presence of a mask. We have used this estimator for estimation of skew-spectrum from individual tomographic bins as well as cross-correlating two different bins. In case of cross-correlation we have used the same mask for the two different bins. Generalization of the PCL method were developed in Munshi et al. (2011a,b,d,e).

In our study, we have used the mask which is shown in Fig. 2. To construct this mask all pixels (shown in maroon) lying within 22 deg of either the galactic or ecliptic planes are discarded. The remaining unmasked pixels cover 14 490 deg^2 of the sky, making fraction of the sky covered $f_{\rm sky} \approx 0.35$ (Taylor et al. 2019). Various aspects of noise involved in cross-correlating CMB lensing maps and galaxy lensing maps are discussed in Fabbian, Lewis & Beck (2019).

Typically, to construct an unbiased PCL estimator the noise contribution is subtracted from the total estimates. This however is not necessary for the construction of the skew-spectrum estimator as the bispectrum of a Gaussian noise is zero. However, presence of noise in the data does increase the variance of the estimator. We will not attempt to construct the covariance matrix of our estimator. Such a generalization will be presented in a future publication.

6 RESULTS

In this section, we discuss the numerical results presented in this paper. We have used all-sky simulations generated at $N_{\rm side} = 4096$ for validating the theoretical predictions. We have used the simulations generated at lower redshifts for weak lensing studies along with the lensing maps generated at $z_s = 1100$ (last scattering surface). Examples of the maps and mask used is presented respectively in Figs 1and 2. We have used these maps for constructing the skew-spectra at individual redshift as well as computing the skew-spectrum by cross-correlating two different redshifts. Below we list our findings.

(i) **Skew-spectra from individual tomographic bins:** First, we compute the theoretical skew-spectra S_ℓ using equation (21) as a function of harmonics ℓ for various smoothing angular scales as well as redshifts. The results for lower redshift bins are plotted in Fig. 3 and the results for the last scattering surface (LSS) is plotted in Fig. 4. In Fig. 3 the panels from left to right correspond to redshifts $z_s = 0.5$, 1.0, 1.5, and 2.0. In each panel three different smoothing angular scales are considered, from top to bottom the curves correspond to FWHM of the Gaussian beam $\theta_s = 0.0$, 5.0, and 10 arcmin as indicated. For the CMB sky shown in Fig. 4 the

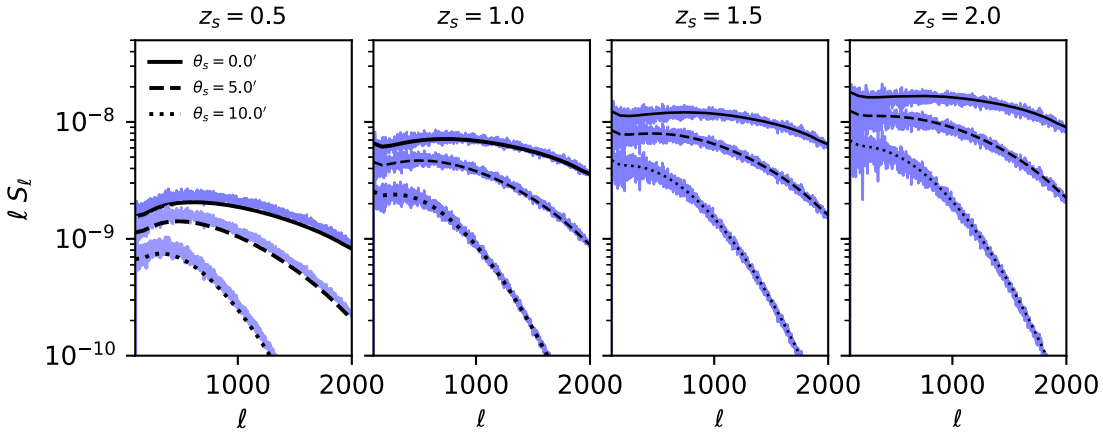

Figure 3. The skew-spectrum S_ℓ defined in equation (21) is being plotted for various smoothing angles and redshifts. The noisy purple lines correspond to results from the simulations. The panels from left to right correspond to redshifts $z_s = 0.5$, 1.0, 1.5, and 2.0. In each panel, we show skew-spectra corresponding to Gaussian beams with full width at half maxima of $\theta_s = 0$, 5, and 10 arcmin, as indicated. We have considered all-sky simulations and no noise was included. The theoretical predictions, shown in black, are computed using the expressions equations (13a)–(13b). The fitting function of Takahasi et al. (2019) was used throughout this study to model the gravity-induced bispectrum B_δ. We use all modes below $\ell_{\rm max} = N_{\rm side}$ in the computation.

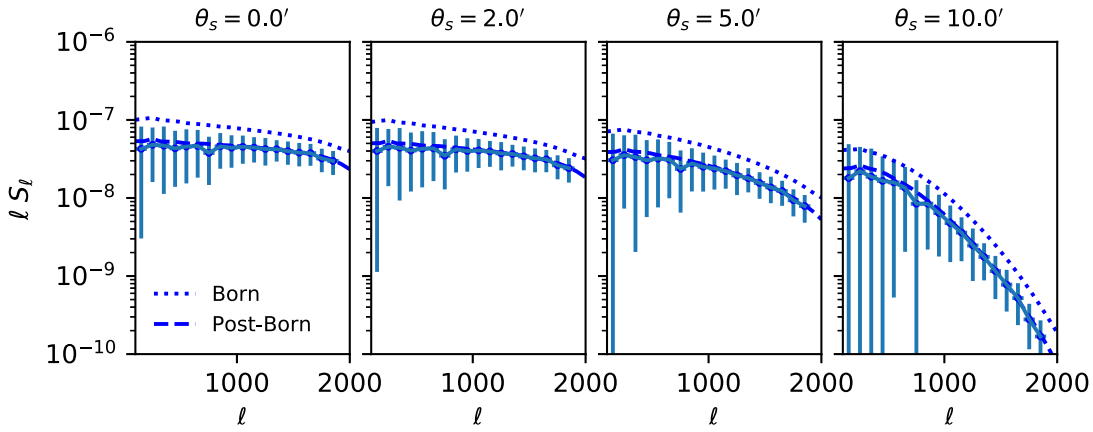

Figure 4. The skew-spectra S_ℓ defined in equation (21) for the CMB is being plotted for various smoothing angles. The smooth dashed and dotted lines correspond to theoretical predictions. The points with error-bars correspond to measurements from numerical simulations. The panels from left to right correspond to various smoothing beams of Full Width at Half Maximum (FWHM) $\theta_s = 0.0$, 2.0, 5.0, and $10'$. respectively. We have considered all-sky simulations and no noise was included. The theoretical predictions are computed using (Takahasi et al. 2019). The dotted curves in each panels are computed using the Born approximation, whereas the dashed curves are computed using more accurate post-Born approximation. The error-bars are computed using ten different realizations of the simulations. The plots underline the importance of post-Born correction in the computation skew-spectrum. Although such corrections can safely be ignored at lower redshifts.

panels from left to right correspond to four different Gaussian beams $\theta_s = 0.0$, 5.0, and 10 arcmin. We have computed the skew-spectra using the Born approximation as well as including the post-Born correction terms (Pratten & Lewis 2016). We found that the post-Born corrections will be important in modelling the skew-spectra at high redshifts. However, for the lower redshifts we found this corrections to be negligible as expected. We have considered all-sky simulations and no noise was included. The theoretical predictions are computed using the expressions in equations (13a)–(13b). The fitting function of Takahasi et al. (2019) was used throughout in this study to model the gravity-induced bispectrum B_δ. We use all modes below $\ell_{\rm max} = 2N_{\rm side}$ in our computation. We have also removed all modes $\ell_{\rm max} < 100$ from our computation. These fitting-functions are found to be an excellent description of the simulated data.

(ii) **Cross-correlating two tomographic bins:** The skew-spectra computed by cross-correlating $\kappa^2(\hat{\Omega})$ and $\kappa(\hat{\Omega})$ from two different redshift bins is being plotted in Figs 5 and 6. In particular, squared $\kappa_1 = \kappa(z_1)$ defined for a source redshift z_1 and $\kappa_2 = \kappa(z_2)$ at redshift z_2 is being cross-correlated in the harmonic domain. For this plot we restrict ourselves to $z_1 > z_2$. We use the expression of mixed bispectrum given in equations (9b)–(9c) for computing the theoretical predictions. The expression for the estimator for the skew-spectrum is given in equation (21). From left to right-hand panels correspond to $z_1 = 2.0$, 1.5 and 1.0 respectively and various curves in each panel correspond to z_2 as indicated. The maps used were constructed at HEALPIX resolution $N_{\rm side} = 4096$. We have filtered all $\ell > 2048$ modes out before analysing them. No additional smoothing was considered. We do not include any noise due to intrinsic ellipticity distribution of galaxies. We have used one single all-sky realization to compute the skew-spectra and no mask was included. The skew-spectra constructed by cross-correlating κ^2 at the Last Scattering Surface (LSS, $z_s = 1100$) and κ at lower redshift is presented in Fig. 7. Similarly, the skew-spectrum constructed using κ at LSS and κ^2 at lower redshift is presented in Fig. 8. We found that the post-Born correction is negligible in modelling the skew-spectrum constructed cross-correlating maps from two redshifts.

(iii) **Accuracy of predictions:** To quantify the difference of predicted skew-spectra and the one estimated from numerical simulation, we have used the following statistics:

$$\Delta_b = \frac{1}{\sigma_b}\left[\hat{S}_b - S_b^{th}\right]. \tag{24}$$

Here $\hat{S}_b$ represents the binned theoretical skew-spectrum and S_b^{th} is the estimated binned skew-spectrum from numerical simulation and σ_b is the standard deviation of the fluctuations in individual ℓ modes within a bin. We have chosen a bin-size of δ_b. The results are shown in Fig. 9. The left-hand panel shows the errors in skew-spectra obtained by cross-correlating $\kappa^2_{\rm LSS}$ and low redshift κ (upper curves) and their symmetric counterparts (lower curves). The fitting functions underpredict the simulation results for $\langle\kappa^2_{\rm LSS}\kappa\rangle$ and underpredict the results for skew-spectra associated with $\langle\kappa_{\rm LSS}\kappa^2\rangle$. The difference between theory and simulation is lowest for $z_s = 0.5$ and increases with the redshift. For $z_s = 2.0$ it can be as high as $1.5\sigma_b$. The results are more pronounced for the intermediate bins. The middle- and right-hand panels of Fig. 9 depicts Δ_b for $\kappa_1^2\kappa_2$ (middle-panel) and $\kappa_2^2\kappa_1$, respectively. The difference is highest for skew-spectra involving $z_s = 0.5$ and lower for higher redshift $z_s = 2.0$. The Δ_b can reach a value of 2.5 for lower redshifts. The theory typically underpredicts the data.

The individual skew-spectral bins are correlated as the skew-spectrum is an integrated measure, i.e. individual ℓ modes (bins) depend on the entire range of ℓ modes (bins). So a straightforward χ^2 analysis (using a diagonal covariance matrix) is not possible. Nevertheless, notice that we have considered noise-free simulations in characterization of errors. Inclusions of noise will increase σ_b and decrease Δ_b. We have considered full-sky maps but, inclusion of the masks will increase the scatter and thus further reduce the value of Δ_b. Hence, the deviations seen here should be seen as a maximum possible deviation for the chosen $N_{\rm side}$.

(iv) **Mask:** We have examined the impact of an *Euclid*-type mask on skew-spectrum in a Pseudo-$\mathcal{C}_\ell$ based approach introduced in Section 5. The results are presented in Fig. 10. The upper solid-lines in each panel correspond to all-sky theoretical predictions of S_ℓ. The upper lines with scatter correspond to the estimates from one realization of the simulated maps. The left-hand panel corresponds to the source redshift $z_s = 1.0$ and the right-hand panel corresponds

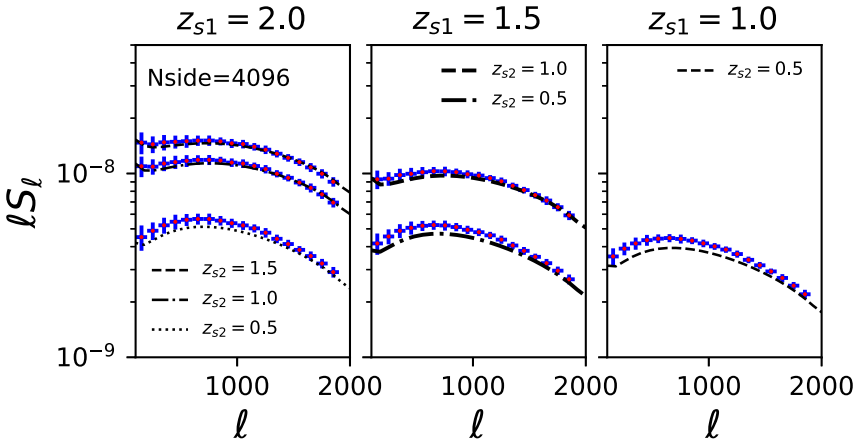

Figure 5. The skew-spectra computed by cross-correlating κ^2 and κ from two different redshift bins is plotted. In particular, the squared $\kappa_1 = \kappa(z_{s1})$ defined for a source redshift z_{s1} and $\kappa_{s2} = \kappa(z_{s2})$ at redshift z_{s2} are being cross-correlated in the harmonic domain. For this plot we restricted ourselves to $z_{s1} > z_{s2}$. The smooth lines correspond to the theoretical predictions and the lines with error bars correspond to results from numerical simulations. We use the expression of *mixed* bispectrum given in equations (9b)–(9c) for computing the theoretical predictions. The expression for the estimator for the skew-spectrum is given in equation (21). The panels from left to right correspond to $z_{s1} = 2.0$, 1.5 and 1.0 respectively and various curves in each panel correspond to z_2 as indicated. The maps used were constructed at Healpix resolution $N_{\rm side} = 4096$. We have filtered all $\ell > 2048$ modes out before analysing them. No additional smoothing was considered. We do not include any noise due to intrinsic ellipticity distribution of galaxies. We have used one single all-sky realization to compute the skew-spectra and no mask was included.

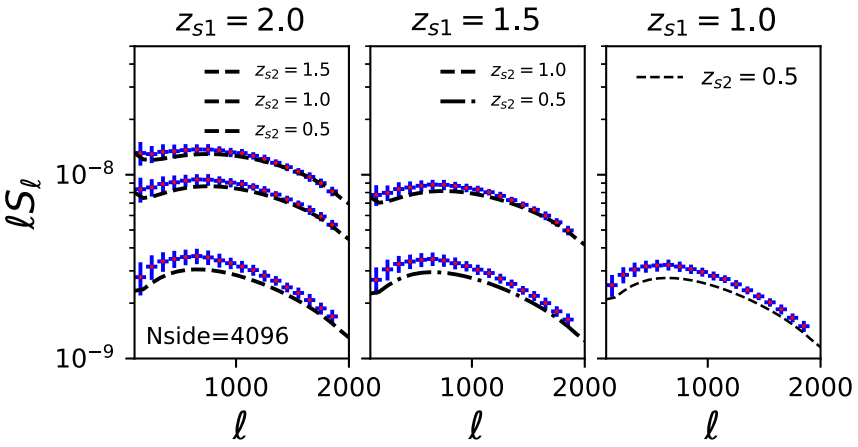

Figure 6. Same as Fig. 5 but the skew-spectrum is being computed cross-correlating κ_1 and κ_2^2 instead of κ_1^2 and κ_2 for $z_{s1} > z_{s2}$.

to $z_s = 2.0$. The lower dashed-curves in each panel correspond to the PCL based theoretical predictions $\tilde{S}_\ell$ computed using equation (22a). The corresponding (lower) lines with scatter are estimates from one realization of partial sky with the *Euclid*-type mask, shown in Fig. 2, applied.

(v) **Noise:** The impact of noise which we assume to be Gaussian on estimation of skew-spectrum is shown in Fig. 11. In both panels the source plane is fixed at $z_s = 1$. The solid lines in each panel represent the theoretical skew-spectrum for $z_s = 1$. The dashed lines represent the pseudo skew-spectrum represented as $\tilde{S}_l$ with an *Euclid*-type mask being included. If we compare the scatter with corresponding plots in Fig. 10 we can see how the inclusion of noise increases the scatter though the estimator remains unbiased. Skew-spectrum for a Gaussian noise alone is zero so the only effect the noise has on the estimator is to increase its scatter.

The noise was generated at each pixel using a Gaussian deviate with variance $\sigma = \sigma_\epsilon/\sqrt{\bar{n}}$. Where we take σ_ϵ represents the variance of the observed ellipticity $\sigma_\epsilon = 0.3$, and $\bar{n}$ is the average number density of source galaxies per pixel computed using total number of observed galaxies, fraction of sky covered and number of pixel at a specific HEALPIX resolution. We have used two different values of $\bar{n}$. The left-hand panel of Fig. 11 corresponds to a source density of $n_s = 30\,\mathrm{arcmin}^{-2}$ and the right-hand panel corresponds to $n_s = 10\,\mathrm{arcmin}^{-2}$. The fraction of the sky covered by the mask was taken to be $f_{\rm sky} = 0.35$.

7 CONCLUSIONS

In this paper, we have introduced the skew-spectrum statistic as a probe for weak lensing bispectrum. While we found an excellent agreement of numerical simulations and fitting-function based theoretical predictions for the autocorrelation we have studied, we also found significant deviation in many other situations and found that the current analytical uncertainty is not sufficient for high accuracy work. We have primarily focused on gravity-induced secondary bispectrum in a ΛCDM cosmology. However, several extensions of our study are possible.

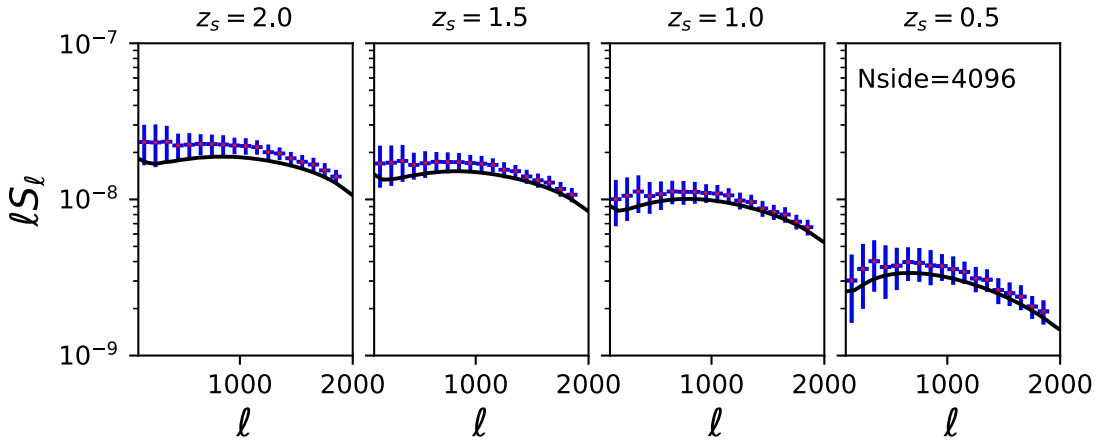

Figure 7. The skew-spectra computed by cross-correlating $\kappa^2_{\rm LSS}$ at the last scattering surface of $z_{\rm LSS} = 1100$ and low redshift weak lensing convergence maps at z_s is being plotted. As before the solid smooth lines in different panels correspond to theoretical results and the lines with error bars correspond to the results from numerical simulations. The panels from left to right correspond to $z_s = 2.0$, 1.5, 1.0, and 0.5, respectively. No mask or smoothing was considered. We use the expression of mixed bispectrum given in equations (9b)–(9c) for computing the theoretical predictions.

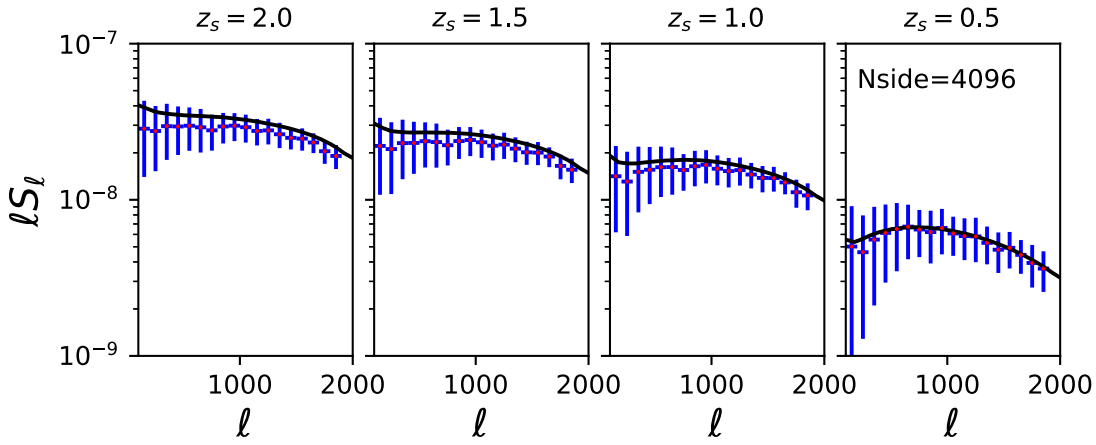

Figure 8. Same as Fig. 7 but are constructed by cross-correlating $\kappa_{\rm LSS}$ against κ^2_s.

7.1 Skew-spectrum in beyond ΛCDM scenarios

In most modified gravity theories and dark energy models, the bispectrum is currently known only in the perturbative regime. We have provided analytical expressions for the skew-spectrum in such scenarios. To go beyond perturbative regime a non-linear model for the bispectrum is required. It is expected that a fitting-function based description in such scenarios will eventually be available as more accurate simulations are performed. Similarly, the modelling of bispectrum based on effective field theories will also be extended to modified gravity theories. Once such results are available, they can readily be used to compute the skew-spectrum in these models.

7.2 Higher order corrections

The theoretical expressions of the skew-spectrum are derived using many simplifying assumptions. We have ignored the corrections due to magnification bias as well as reduced shear which should be included in more accurate theoretical predictions. In addition, the skew-spectrum here is computed using the Limber approximation (Kitching et al. 2017).

7.3 Skew-spectrum from shear maps

We have computed the skew-spectrum from a convergence map. However, for many practical purposes a skew-spectrum estimated directly from shear maps can bypass many of complications of the map making process.

7.4 Intrinsic alignment

The intrinsic alignment (IA) of galaxies (see Vlah, Chisari & Schmidt 1910, and the references therein) are caused by the tidal interaction and is a source of contamination to gravity-induced (extrinsic) weak lensing. The lensing bispectrum induced by IA is typically at the level of 10 per cent of the lensing induced bispectrum. Several methods have been proposed to mitigate or remove such contamination using joint analysis of power spectrum and bispectrum. The skew-spectrum retains some of the shape information of the original bispectrum. A joint analysis of power spectrum and skew-spectrum can thus be useful in separation of these two different contributions. The skew-spectrum introduced in this study can further be optimized by introducing weights to judge the level of cross-contamination from the intrinsic alignment much in the same way as was achieved

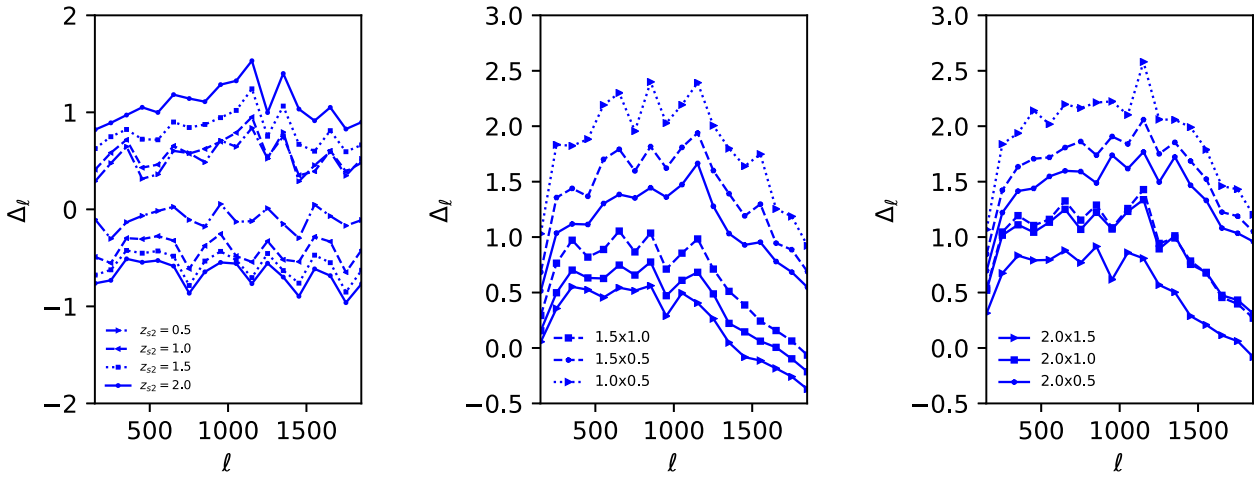

Figure 9. In this figure we present the accuracy of the fitting function we have used in our study. We have used the binned skew-spectra for our comparison. A bin-size of $\delta_b = 100$ is being used. Here Δ_ℓ represents the normalized deviation from predictions and results from simulations (see the text for details). The left-hand panel corresponds to the skew-spectrum computed by cross-correlating the CMB sky and the low redshift weak lensing The middle- and the right-hand panel correspond to the skew-spectra obtained by cross-correlating two tomographic lensing maps. The plots in the left-hand panel are obtained using the results presented in the Figs 7 and 8. The upper set of curves correspond to the cross-correlation of tomographic bins against convergence map at $z_{\rm LSS}$ i.e. $\langle \kappa^{\,2}(z_s)\kappa_{\rm LSS}\rangle$, whereas the lower curves correspond to their symmetric counterparts $\langle \kappa(z_s)\kappa^2_{\rm LSS}\rangle$. The error in skew-spectra computed using lower redshift maps that are associated with $\langle \kappa^{\,2}(z)\kappa_{\rm LSS}\rangle$ are depicted in the middle panel. Their symmetric counterparts are shown in the right-hand panel. The line-styles used in the middle and right-hand panels are identical. For the corresponding skew-spectra see Figs 5 and 6, respectively.

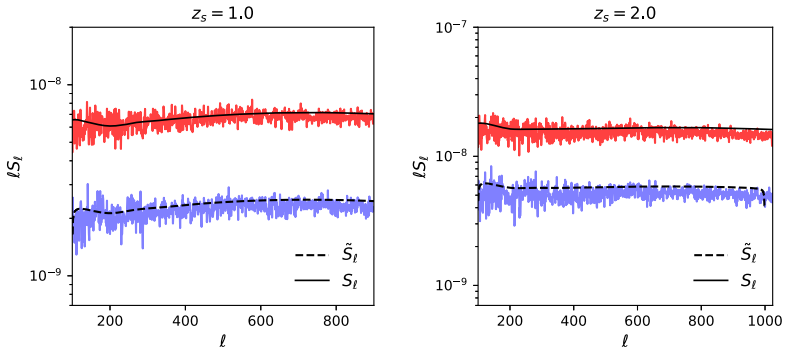

Figure 10. The pseudo-$\mathcal{S}_\ell$ for two different redshifts are presented. A *Euclid*-type mask was used in our study. The regions which are within 22 deg of the galactic or ecliptic plane are removed from our study. The fraction of the sky left unmasked is $f_{\rm sky} = 0.35$ (roughly 14 490 deg^2 of the sky). The left-hand (right) panel corresponds to $z_s = 1.0 (z_s = 2.0)$. The upper smooth solid curves represents the theoretical S_ℓ. The two upper curves represent estimated skew-spectrum from a single realization. The curve that shows more scatter represents skew-spectrum estimated from an all-*sky* map. The curve which shows more scatter correspond to $\hat{S}_\ell$ using equation (22a).

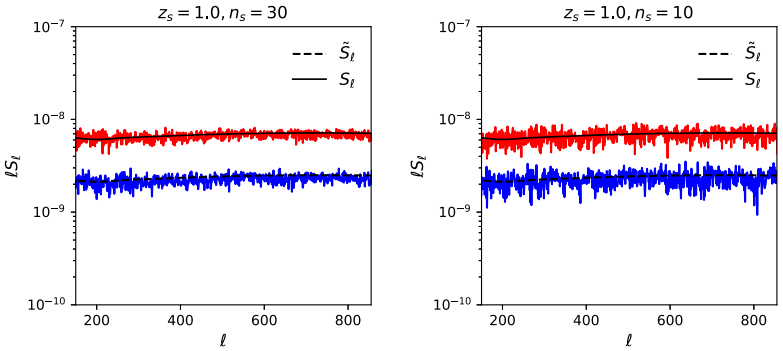

Figure 11. The impact of noise (assumed Gaussian) on estimation of skew-spectrum is presented. In both panels the source plane is fixed at $z_s = 1$. The solid lines in each panel represent the theoretical skew-spectrum for $z_s = 1$. The dashed line represent the pseudo skew-spectrum or $\tilde{S}_l$ for the *Euclid*-type mask being considered. Inclusion of Gaussian noise increases the scatter but the estimator remains unbiased. The left-hand panel corresponds to source density of $n_s = 30\,\text{arcmin}^{-2}$ and the right-hand panel corresponds to $n_s = 10\,\text{arcmin}^{-2}$.

in case of point source contamination of CMB studies designed to detect primordial non-Gaussianity from Planck data.

7.5 Primordial non-Gaussianity and active perturbations

We have considered the gravity-induced non-Gaussianity in our study as it is the most dominant source of non-Gaussianity in weak lensing maps. However, similar results can also obtained for computing the subdominant contributions from primordial non-Gaussianity as well as secondary sources of non-Gaussianity induced by active sources, e.g. cosmic strings.

7.6 Baryonic feedback

We have not included any baryonic feedback in our modelling of the skew-spectrum but such corrections can be incorporated in the skew-spectrum for direct comparison with any realistic data.

7.7 Covariance and likelihood

We have not discussed the covariance of the skew-spectrum in this study. An accurate description of the covariance will be an important ingredient of cosmological likelihood analysis involving skew-spectrum. A simple form of covariance can be derived under the assumption of Gaussianity and thus ignoring all higher order correlation contributing to the covariance. Such an estimation will be useful in the noise-dominated regime but will not be sufficient in the highly non-linear scales characterized by high signal-to-noise probed by the future surveys such as *Euclid*. The methods developed so far in computing the covariance include the ones based on perturbative analysis, halo model, or simulated mocks (Rizzato et al. 2019). These methods can be adapted to compute the skew-spectrum covariance.

ACKNOWLEDGEMENTS

DM is supported by a grant from the Leverhume Trust at MSSL. It is a pleasure for DM to thank Filippo Vernizzi for useful discussion. We would like to thank Peter Taylor for providing us his code to generate the Euclid type mask used in our study as well as for many useful discussions. We would like to thank Ryuichi Takahashi for careful reading of the draft and suggestions for improvements.

DATA AVAILABILITY

No new data were generated in support of this research. The simulations used in this work are publicly available.

REFERENCES

Amendola L. et al., 2013, Living Rev. Relat., 16, 6
Bartolo N., Komatsu E., Matarrese S., Riotto A., 2004, Phys. Rep., 402, 103
Baumann D., Nicolis A., Senatore L., Zaldarriaga M., 2012, J. Cosmol. Astropart. Phys., 1207, 051
Bernardeau F., 1994a, A&A, 291, 697
Bernardeau F., 1994b, A&A, 291, 697
Bernardeau F., 1996, A&A, 312, 11
Bernardeau F., Colombi S., Gaztanaga F., Scoccimarro R., 2002, Phys. Rep., 367, 1
Bernardeau F., Mellier Y., van Waerbeke J., 2002, A&A, 389, L28
Bernardeau F., van Waerbeke L., Mellier Y., 2003, A&A, 397, 405
Calabrese E., J. Smidt J., Amblard A., Cooray A., Melchiorri A., Serra P., Heavens A., Munshi D., 2010, Phys. Rev. D, 81, 3529
Clifton T., Ferreira P. G., Padilla A., Skordis C., 2012, Phys. Rep., 513, 1
Codis S., Pichon C., Bernardeau F., Uhlemann C., Prunet S., 2016, MNRAS, 460, 1549
Cooray A., 2001, Phys. Rev. D, 64, 043516
Cooray A., Sheth R., 2002, Phys. Rep., 372, 1
Dai J.-P., Verde L., Xia J.-Q., 2019, preprint (arXiv:2002.09904)
Dizgah M. A., Lee H., Schmittfull M., Dvorkin C., 2020, J. Cosmol. Astropart. Phys., 04, 011
Drinkwater M. J. et al., 2010, MNRAS, 401, 1429
Efstathiou G., 2004, MNRAS, 349, 603
Eggemeier A., Smith R. E., 2017, MNRAS, 466, 2496
Eisenstein D. J. et al., 2011, AJ, 142, 72
Fabbian G., Lewis A., Beck D., 2019, J. Cosmol. Astropart. Phys., 10, 057
Gil-Marn H., Wagner C., Fragkoudi F., Jimenez R., Verde L., 2012, JCAP, 02, 057
Gorski K. M., Hivon E., Banday A. J., Wandelt B. D., Hansen F. K., Reinecke M., Bartelman M., 2005, ApJ, 622, 759
Gruen D. et al., 2018, Phys. Rev. D, 98, 023507
Harrison I., Coles P., 2011, MNRAS, 418, L20
Hivon E., Gorski K. M., Netterfield B., Crill B. P., Prunet S., Hansen F., 2002, ApJ, 567, 2
Joyce A., Jain B., Khoury J., Trodden M., 2015, Phys. Rep., 568, 1
Kacprzak T. et al., 2016, MNRAS, 463, 3653
Kilbinger M. et al., 2017, MNRAS, 472, 2126
Kitching T. D., Alsing J., Heavens A. F., Jimenez R., McEwen J. D., Verde L., 2017, MNRAS, 469, 2737
Komatsu E., Spergel D. N., Wandelt B. D., 2005, ApJ, 634, 14
Krause E., Chang T.-C., Doré O., Umetsu K., 2013, ApJ, 762, L20
Kuijken K. et al., 2015, MNRAS, 454, 3500
Laureijs R. et al., 2011, ESA/SRE(2011)12, preprint (arXiv:1110.3193)
Lesgourgues J., Pastor S., 2006, Physics Reports, 429, 307
Munshi D., 2000, MNRAS, 318, 145
Munshi D., Heavens A., 2010, MNRAS, 401, 2406
Munshi D., Jain B., 2001, MNRAS, 322, 107
Munshi D., McEwen J. D., 2020, preprint (arXiv:2004.07021)
Munshi D., Regan D., 2012, J. Cosmol. Astropart. Phys., 06, 042
Munshi D., Jain B., 2000, MNRAS, 318, 109
Munshi D., Valageas P., Van Waerbeke L., Heavens A., 2008, Phys. Rep., 462, 67
Munshi D., Heavens A., Cooray A., Smidt J., Coles P., Serra P., 2011a, MNRAS, 412, 1993
Munshi D., Coles P., Cooray A., Heavens A., Smidt J., 2011b, MNRAS, 414, 3173
Munshi D., Smidt J., Heavens A., Coles P., Cooray A., 2011d, MNRAS, 411, 2241
Munshi D., Kitching T., Heavens A., Coles P., 2011e, MNRAS, 416, 629
Munshi D., van Waerbeke L., Smidt J., Coles P., 2012, MNRAS, 419, 536
Munshi D., Namikawa T., Kitching T. D., McEwen J. D., Takahashi R., Bouchet F. R., Taruya A., Bose B., 2020a, MNRAS, 493, 3985
Munshi D., McEwen J. D., Kitching T., Fosalba P., Teyssier R., Stadel J., 2020b, JCAP, 05, 043
Namikawa T., Bose B., Bouchet F. R., Takahashi R., Taruya A., 2019, Phys. Rev. D, 99, 063511
National Research Council, 2010, New Worlds, New Horizons in Astronomy and Astrophysics. The National Academies Press
Oh S. P., Spergel D. N., Hinshaw G., 1990, ApJ, 510, 551
Planck Collaboration, 2014, A&A, 571, A16
Planck Collaboration XIII 2016a, A&A, 594, 17
Planck Collaboration XIII 2016b, A&A, 594, A13
Planck Collaboration VI 2018, preprint (arXiv:1807.06205)
Pratten G., Lewis A., 2016, J. Cosmol. Astropart. Part., 08, 047
Pratten G., Munshi D., 2012, MNRAS, 423, 3209
Rizzato M., Benabed K., Bernardeau F., Lacasa F., 2019, MNRAS, 490, 4688
Schmittfull M., Baldauf T., Seljak U., 2015, Phys. Rev. D, 91, 043530
Scoccimarro R, Frieman J. A., 1999, ApJ, 520, 35
Shan H. et al., 2018, MNRAS, 474, 1116
Smidt J., Amblard A., Byrnes C. T., Cooray A., Heavens A., Munshi D., 2010, PRD, 81, 123007

Szapudi I., Prunet S., Pogosyan D., Szalay A. S., Bond J. R., 2001, ApJ, 548, 115
Takahashi R., Hamana T., Shirasaki M., Namikawa T., Nishimichi T., Osato K., Shiroyama K., 2017, ApJ, 850, 24
Takahashi R. et al., 2020, ApJ, 895, 113
Taylor P. L., Kitching T. D., Alsing J., Wandelt B. D., Feeney S. M., McEwen J. D., 2019, Phys. Rev. D, 100, 023519
The Dark Energy Survey Collaboration, 2016, Phys. Rev. D, 94, 022001
Tyson J. A., Wittman D. M., Hennawi J. F., Spergel D. N., 2003, Nucl. Phys. B, 124, 21
Uhlemann C., Codis S., Pichon C., Bernardeau F., Reimberg P., 2016, MNRAS, 460, 1529
Valageas P., 2002, A&A, 382, 412
Vlah Z., Chisari N. E., Schmidt F., 1910, preprint (arXiv:1910.08085)

This paper has been typeset from a TEX/LATEX file prepared by the author.